

TIC65910228b: A single-transit discovery of a massive long-period warm Jupiter with TESS

Felipe I. Rojas¹, Rafael Brahm^{2,3}, Matías I. Jones⁴, Márcio Catelan^{1,3}, Jozef Liptak^{7,8}, Lorena Acuña⁵, Jan Eberhardt⁵, Néstor Espinoza⁶, Thomas Henning⁵, Andrés Jordán^{2,3}, Yared Reinarz⁵, Marcelo Tala Pinto⁹, Trifon Trifonov^{5,10,11}, Michaela Vítková^{7,12}, Luca Antonucci^{13,14}, Gaspar Bakos¹⁵, Attila Bódi¹⁵, Gavin Boyle^{16,17}, Zoltán Csabry¹⁵, Joel Hartman¹⁵, Jan Janík¹², Petr Kabáth⁷, Anthony Keyes¹⁵, Markus Roth¹⁸, Petr Škoda⁷, Alton Spencer¹⁹, Vincent Suc^{2,3,16}, Geert Jan Talens²⁰, Jan Vaclavík²¹, and Leonardo Vanzi^{13,14}

(Affiliations can be found after the references)

Received January 31, 2026

ABSTRACT

Context. Warm Jupiters are excellent case studies for the investigation of giant planet internal structures and formation theories. However, the sample of long-period transiting giants is still small today for a better understanding of this population.

Aims. Starting from a single transit found in the Transiting Exoplanet Survey Satellite (TESS) data, we confirm the planetary nature of the signal and measure its orbital parameters, mass, and radius. We put this system in the context of long-period giant transiting planets and analyzed the viability to sustain atmospheric or dynamical follow-up.

Methods. We carried out a spectroscopic follow-up using FEROS and PLATOSpec to obtain precise radial velocities. We added a photometric follow-up with HATPI and Observatoire Moana to obtain a more precise estimate of the orbital period. We derived the orbital and physical parameters through a joint analysis of this data.

Results. We report the discovery and characterization of TIC65910228b, a transiting warm Jupiter with a mass of $4.554 \pm 0.255 M_J$ and a radius of $1.088 \pm 0.061 R_J$, orbiting an evolved F-type star every ~ 180.52 days in an eccentric orbit ($e = 0.25 \pm 0.04$).

Conclusions. This planet joins a still under-explored population of long-period ($P > 100$) massive ($M_p > 4 M_J$) transiting giant planets, being one of the few with a mild eccentricity. This target is a nice example of the potential of single-transit events to populate this region of the parameter space.

Key words. Planets and satellites: detection – Planets and satellites: fundamental parameters – Planets and satellites: general

1. Introduction

In recent decades, thousands of exoplanets have been discovered. Among these, warm Jupiters (WJ; radii greater than four times Earth's and orbital periods longer than 10 days) represent a valuable sample for studying the formation and evolution of planetary systems. Unlike hot Jupiters (HJ; Mayor & Queloz 1995), warm Jupiters are located far enough from their host stars to avoid inflation caused by stellar irradiation, which complicates internal structure studies (e.g. Thorngren et al. 2016; Fortney et al. 2021; Acuña et al. 2024), as the proposed mechanisms are not well understood (Sarkis et al. 2021). This distance also prevents tidal circularization, a process that can alter their original orbital parameters, such as eccentricity and obliquity, which provide insights into their formation and migration scenarios (Albrecht et al. 2022). In this context, different mechanisms have been proposed that could explain the observed population of warm Jupiters (e.g. Goldreich & Tremaine 1980; Rasio & Ford 1996; Boley et al. 2016; Kozai 1962; Lidov 1962; Lithwick & Wu 2011). Their mass, size, and orbital period make them ideal targets for combining transit and radial velocity observations around bright stars.

Since its launch in 2018, the Transiting Exoplanet Survey Satellite (TESS; Ricker et al. 2014) has been surveying the entire sky in search of transiting exoplanets, focusing on regions of 24 by 96 degrees every 27 days. However, as the orbital period increases, the likelihood of observing a transit decreases,

posing a significant challenge for characterizing systems with long orbital periods. Given this strategy, most warm Jupiters in TESS are expected to be observed as single transiting events or with interrupted observations, preventing a direct measurement of their orbital periods. Simulations show that 76% of warm Jupiters with periods longer than 100 days should be observed as single transits in years 1 – 3 (Rodel et al. 2024). In the first two years of data, it is expected that between 500 and 1000 single-transit events will be observed (Cooke et al. 2018; Villanueva et al. 2019).

To overcome this challenge, the Warm gIaNs with TESS (WINE) collaboration has been aiming to identify and characterize such planets through ground-based follow-up observations of TESS candidates (Brahm et al. 2023; Jones et al. 2024; Eberhardt et al. 2025). In particular, for single transits, spectroscopic monitoring is crucial to constrain the orbital period if no additional transits are found and to rule out false-positive scenarios.

In this study, we present the discovery and detailed characterization of TIC65910228b, a warm Jupiter orbiting an evolved F-type star with an orbital period of 180.5 days. The planet was first detected as a single-transit signal in TESS data and later confirmed through high-precision radial velocity measurements from FEROS and PLATOSpec, along with follow-up ground-based transit observations conducted with HATPI and at Observatoire Moana. This system constitutes an important addition to

Table 1: Summary of ground-based follow-up observations.

Telescope	Filter	Coverage	Date
TESS Sector 33	TESS	Full	2018/12/18 to 2019/01/13
HATPI	Asahi Spectra 430–890 nm	Egress	2024/12/09
OM-ES1	r	Egress	2025/12/05
<hr/>			
Instrument	Observations	Date	
FEROS	6	2024/12/10 — 2025/03/30	
PLATOSpec	42	2024/12/13 — 2026/01/05	

the still limited sample of well-characterized warm Jupiters with accurately determined masses and radii.

The paper is structured as follows: In Section 2, we present the photometric and spectroscopic data that were collected. Section 3 outlines the analysis conducted on this data. The results and discussion are provided in Section 4, and we conclude with a summary in Section 5.

2. Observations

Besides the data from TESS, a photometric follow-up from the ground is needed to i) have a more precise constraint on the period and ii) observe the transit with better resolution to confirm the origin of the signal and discard blended scenarios. A spectroscopic follow-up was also performed to measure precise radial velocities and characterize the stellar host.

A summary of the photometric and spectroscopic observations used in the analysis can be found in Table 1.

2.1. Photometry

2.1.1. TESS

TIC65910228 was observed during the first year of TESS Mission (Ricker et al. 2014) in Sector 7, with a cadence of 30 minutes. During the first extended mission, observations were conducted in Sectors 33 and 34 at a 10-minute cadence. In the second extended mission, it was observed in Sector 61 with a cadence of 2 minutes. In year 7, it was observed in Sectors 87 and 88.

A single transit was identified in Sector 33 and reported as a CTOI in the Exoplanet Follow-up Observation Program (ExoFOP; DOI: 10.26134/ExoFOP5). TESS-SPOC (Caldwell et al. 2020) light curve from Sector 33 was employed for this analysis, in particular using the PDCSAP flux.

Figure 1 shows the TESS field of TIC65910228 in Sector 33 with Gaia (Gaia Collaboration et al. 2021) sources overplotted and the aperture used in the TESS-SPOC light curve. The light curve is plotted in Figure 5.

2.1.2. HATPI

HATPI is a wide-field photometric instrument located at Las Campanas Observatory (LCO). The HATPI system comprises a mosaic of 64 identical camera-lens units mounted together on a single platform, enabling continuous imaging of the entire sky

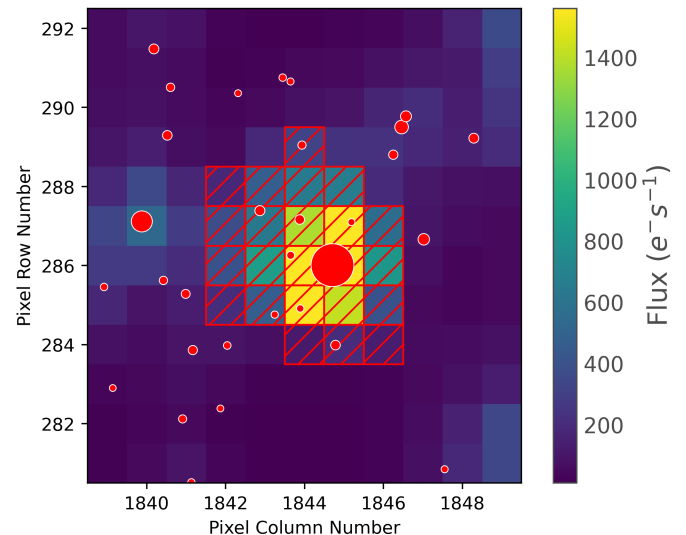


Fig. 1: TESS Target Pixel File preview of TIC65910228. Aperture used in TESS-SPOC light curve corresponds to the overplotted red dashed area. Gaia DR3 sources up to 7 magnitudes of difference are overplotted in red dots. Dot size is proportional to brightness.

visible from LCO with cadences of 30 and 45 seconds and a pixel scale of 20 arcsec pix^{-1} (Bakos et al., 2025, in preparation).

High-precision light curves were generated using aperture and image subtraction photometry. This data is available in three formats: raw photometry, detrended via External Parameter Decorrelation (EPD) and with systematic correction using Trend Filtering Algorithm (TFA; Kovács et al. 2005) in the EPD light curve. EPD removes variability that correlates with instrumental and non-astrophysical variables, in this case the image position of the source, the horizontal angle, the airmass and the shape of the point-spread function. We used the subtracted photometry TFA light curve for this work.

The target was observed in three different seasons, with light curves that spans from 2022/08/17 to 2023/06/02, 2023/08/17 to 2024/06/02, and 2024/08/17 to 2025/06/02. An egress of a TIC65910228b transit was observed by HATPI on December 9, 2024, which is consistent with the period found in Section 3.2.

2.1.3. Observatoire Moana

Another egress from TIC65910228b was observed on December 5, 2025, with a robotic 60 cm telescope located at El Sauce station of Observatoire Moana (OM-ES). The telescope is equipped with a 2048×2048 pixel detector, providing a pixel scale of 0.7 arcsec pix^{-1} . Observations were carried out in the r' band, with exposures every 50 seconds.

The reduction process was carried out using an automated pipeline that integrates all available sources within the field. This generates light curves and artificial comparison stars for all qualifying sources, accounting for variability and magnitude differences. Additionally, it uses an optimization algorithm that accounts for the spatial separation between the targets and other sources.

This egress was predicted using previous analysis with HATPI data and radial velocities, which allowed us to constrain the period and refine the ephemeris to schedule the observations.

2.2. Radial Velocities

2.2.1. FEROS

Six observations were conducted with the FEROS spectrograph (Kaufer et al. 1999) mounted at the 2.2m MPG telescope in La Silla Observatory. The adopted exposure time was 900 seconds. Data were observed between December 10, 2024, and March 30, 2025.

Data were processed using the CERES pipeline (Brahm et al. 2017a), which calculates the cross-correlation function (CCF), obtaining precision radial velocities, bisector span, and full width at half maximum (FWHM) of the CCF. The spectra obtained had a mean signal-to-noise ratio of 84.

2.2.2. PLATOSpec

We observed TIC65910228 42 times with PLATOSpec (Kabáth et al. 2025) between December 13, 2024, and January 5, 2026. PLATOSpec is a high-resolution fiber-fed echelle spectrograph designed to support space missions such as PLATO and Ariel. It is installed in the 1.52m telescope at La Silla Observatory, covering a spectral range of 380 to 680 nm with a resolving power of $R = 70000$. The exposures lasted 900 seconds, yielding a mean signal-to-noise ratio of 53.

Observations were reduced using the CERES pipeline, measuring radial velocities, bisector span, and FWHM.

3. Analysis

3.1. Stellar Parameters

For the spectroscopic properties, we followed the same procedure in (Brahm et al. 2019). The first step consisted of analyzing the co-added spectra to derive T_{eff} , $\log g$, $[\text{Fe}/\text{H}]$, and $v \sin i$. This is done using the ZASPE package Brahm et al. (2017b), which determines these parameters by comparing the data with a grid of synthetic spectral models.

After this, we performed a spectral energy distribution (SED) fit using available broad-band photometry, in combination with `parsec` stellar evolutionary models (Bressan et al. 2012) and parallax from Gaia DR3 (Gaia Collaboration et al. 2023). In this stage, the previously derived T_{eff} was used as a prior, while the metallicity is fixed. In this way, we obtain an improved estimate of the surface gravity, which is then fixed for another iteration of ZASPE.

These two steps were repeated until convergence was reached. From this analysis, we found that TIC65910228 is an F-type metal-rich evolved star.

Table 2 resumes all stellar parameters found in the literature and derived from the high-resolution spectra. These results were adjusted according to the guidelines in Tayar et al. (2022), where uncertainties of T_{eff} , L_{\star} , R_{\star} , M_{\star} and age have been raised by 2.4%, 2%, 4.2%, 5%, and 20% in quadrature, respectively.

3.2. Periodical signals and stellar activity

We calculated the generalized Lomb–Scargle periodogram (Zechmeister & Kürster 2009) for the PLATOSpec observations to search for periodical signals. The periodogram displays a prominent peak at approximately 180 days. Additionally, we calculated the periodogram for the bisector span and the FWHM, as these quantities serve as proxies for stellar activity.

Figure 2 shows the periodogram of radial velocities, bisector span, and FWHM derived from the PLATOSpec observations,

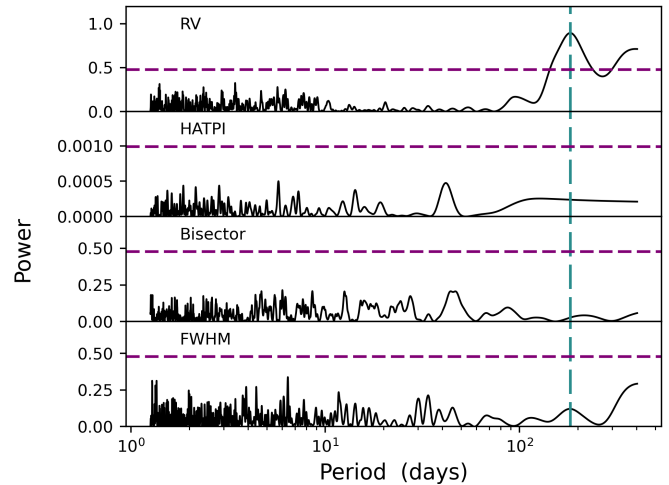


Fig. 2: Periodograms displaying periodic signals in the radial velocities, HATPI photometry, radial-velocity bisector span and radial-velocity FWHM. The green vertical line indicates the optimal period derived from radial-velocity data. Horizontal dashed line corresponds to the 1% false alarm probability.

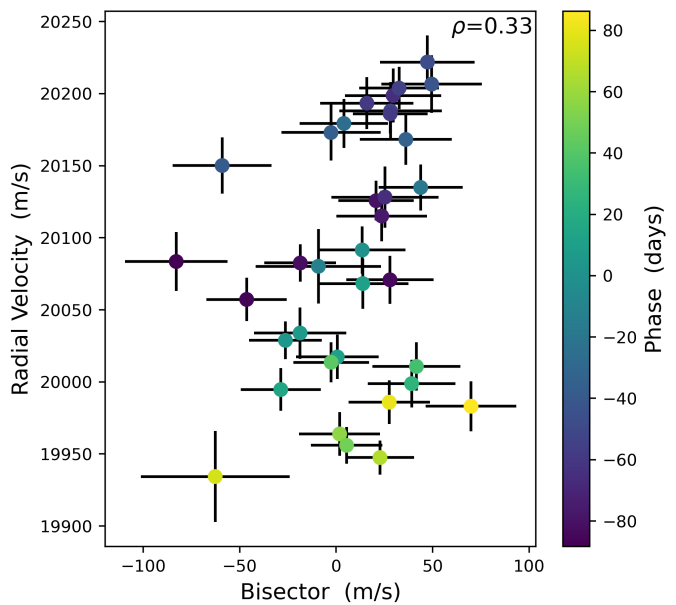


Fig. 3: Bisector vs radial velocity scatter plot. Spearman's rank correlation coefficient ρ shows no significant correlation between the two variables, ruling out the possibility that the RV signal has an activity origin traced by the Bisector.

together with the GLS periodogram of the HATPI light curve, which can uncover variability linked to stellar rotation.

The absence of notable features in the activity indicators, aligned with those detected in the radial velocity data, indicates that the observed signal is most likely of planetary origin. Also, bisectors don't show a significant correlation with radial velocities (see Figure 3).

Table 2: Stellar parameters of TIC65910228.

Parameter		Source
Identifying Information		
TIC ID	TIC65910228	TIC ^a
GAIA ID	5606317297918628992	Gaia EDR3 ^b
2MASS ID	J07145152-2925498	2MASS ^c
R.A. (J2015.5, h:m:s)	7 ^h 14 ^m 51.52 ^s	Gaia EDR3 ^b
DEC (J2015.5, d:m:s)	-29°25'49.91"	Gaia EDR3 ^b
Proper motion and parallax		
$\mu_\alpha \cos \delta$ (mas yr ⁻¹)	-13.566 ± 0.011	Gaia EDR3 ^b
μ_δ (mas yr ⁻¹)	-21.083 ± 0.013	Gaia EDR3 ^b
Parallax (mas)	3.74 ± 0.013	Gaia EDR3 ^b
Spectroscopic properties		
T_{eff} (K)	6235.0 ⁺¹⁷⁵ ₋₁₇₅	ZASPE ^d
Spectral Type	F	ZASPE ^d
[Fe/H] (dex)	0.14 ^{+0.05} _{-0.05}	ZASPE ^d
$\log g_*$ (cgs)	4.043 ^{+0.02} _{-0.02}	ZASPE ^d
$v \sin(i_*)$ (km/s)	8.7 ^{+0.5} _{-0.5}	ZASPE ^d
Photometric properties		
T (mag)	9.734 ± 0.004	TIC ^a
G (mag)	10.110 ± 0.0003	Gaia EDR3 ^b
B (mag)	10.819 ± 0.064	Tycho-2 ^e
V (mag)	10.225 ± 0.004	Tycho-2 ^e
J (mag)	9.251 ± 0.026	2MASS ^c
H (mag)	9.01 ± 0.026	2MASS ^c
Ks (mag)	8.938 ± 0.023	2MASS ^c
Derived properties		
M_* (M_\odot)	1.386 ^{+0.071} _{-0.071}	PARSEC*
R_* (R_\odot)	1.856 ^{+0.079} _{-0.079}	PARSEC*
L_* (L_\odot)	4.7 ^{+0.2} _{-0.2}	PARSEC*
A_v (mag)	0.08 ^{+0.05} _{-0.05}	PARSEC*
Age (Gyr)	2.8 ^{+0.6} _{-0.6}	PARSEC*
ρ_* (g cm ⁻³)	306 ⁺⁴⁶ ₋₃₉	PARSEC*

Notes. Logarithms given in base 10.

^(a) TESS Input Catalog (Stassun et al. 2018) ; ^(b) Gaia Early Data Release 3 (Gaia Collaboration et al. 2021) ;^(c) Two-micron All Sky Survey (Skrutskie et al. 2006) ;^(d) Zonal Atmospheric Stellar Parameters Estimator (Brahm et al. 2019, 2017b) ;^(e) Tycho-2 Catalog (Høg et al. 2000)

*: PARSEC isochrones (Bressan et al. 2012); using stellar parameters obtained from ZASPE.

3.3. Joint-fit

We performed a joint fit of all the collected TIC65910228b data using `juliet`. This software relies on nested sampling (NS; Skilling 2004) and incorporates several state-of-the-art models and tools. In particular, we used `batman` (Kreidberg 2015) to model the transits, `radvel` (Fulton et al. 2018) for the radial-velocity data, and `george` (Ambikasaran et al. 2015) together with `celerite` (Foreman-Mackey et al. 2017) to describe the Gaussian processes (GP). Nested sampling was carried out with the `dynesty` library (Speagle 2020) with 1000 live points.

The orbital parameters used for the model were the orbital period P , the ephemeris of the transit t_0 , stellar density ρ_* (instead of a/R_*), radial velocity semi-amplitude K , orbital eccentricity e , and argument of periastron passage ω . We adopted the r_1 , r_2 parametrization from (Espinoza 2018) instead of fitting

the planet-to-star radius ratio R_p/R_{star} and the impact parameter b directly.

In addition, instrumental parameters are required to account for the different properties of each dataset, in this case: the dilution factor D , relative flux offset m_F , limb darkening parameters, systemic radial velocity μ , jitter parameters, and possible terms that account for light curve variability.

The TESS Sector 33 light curve was resampled to a 1.6-minute cadence following the method described by Kipping (2010) to correct for morphological distortions caused by the integration time.

3.3.1. Dilution

Due to the relatively large pixel scales of TESS (21 arcsec pix⁻¹) and HATPI (19.7 arcsec pix⁻¹), a dilution factor is typically included to account for crowding effects. However, since we used

the PDCSAP_FLUX from the TESS–SPOC light curves, no additional correction is required, as these fluxes are already adjusted for crowding. For HATPI, we adopted a uniform prior between 0.8 and 1, as it is expected that the dilution from this instrument shouldn't exceed 10%. In contrast, OM-ES1 photometry is primarily limited by seeing, therefore, we fixed the dilution factor to 1 in this case.

3.3.2. Limb darkening

Following the recommendations of (Espinoza & Jordán 2016), we adopted a quadratic law for the transit fitting of all the photometric data, adopting the parametrization proposed by (Kipping 2013). These parameters q_1 and q_2 are inherent to each filter and instrument, so all three photometric sets have independent ones.

3.3.3. Jitter and variability

Jitter terms σ are included for each instrument to address possible underestimated error bars and unknown sources that introduce variability in both photometry and radial velocity.

For photometry in particular, additional parameters were added to account for long-term trends. For TESS, a GP over time with a Matern 3/2 kernel was employed to model variations in the out-of-transit flux (see Figure 4).

3.4. Model selection

As nested sampling estimates the Bayesian evidence, it provides a procedure for comparing different models, with the one with the highest evidence being favored. In the context of this paper, we compared the following main models:

- i No planet: The variations in RV are explained just by noise
- ii 1 eccentric planet: The RV signal is explained by a single planet. Eccentricity is left as a free parameter.
- iii 1 eccentric planet + RV linear trend: Same as before, but adding a linear trend to the Keplerian model, coming from an external companion with a period much longer than the baseline of observations.

Using Bayesian evidence, model ii is favored over model iii with a $\Delta Z = 2.2$. Although the difference is not significant, model ii is the simplest option and thus is selected. The best-fit model was subtracted from the radial velocity data, and the residuals were analyzed with a GLS periodogram, which showed no additional periodic signals (see Figure 7).

4. Results

The analysis confirms that TIC65910228 is an evolved F-type star hosting a warm giant planet. This planet has a mass of $M_p = 4.554^{+0.255}_{-0.247} M_J$, a radius of $R_p = 1.088^{+0.061}_{-0.057} R_J$, and a bulk density of $\rho_p = 4.374^{+0.800}_{-0.674} \text{ g cm}^{-3}$. The planet is in a mildly eccentric orbit with $e = 0.25^{+0.03}_{-0.04}$ with a period of $P = 180.524140^{+0.000978}_{-0.001048}$ days.

Results from the posterior distributions of the joint-fit are summarized in Table 3. Best model fits of the transits can be seen in Figure 5 and for radial velocities in Figure 6. All derived parameters are listed in Table 4.

4.1. Interior modelling

We computed interior models of TIC65910228b using the Modules for Experiments in Stellar Astrophysics (MESA; Paxton et al. 2011, 2013), following the methodology presented in Jones et al. (2024) and Tala Pinto et al. (2025). In this case, we modeled the planet with an inert isodensity core with different masses, surrounded by a gaseous envelope with different metallicity values. For the core, we used a 1:1 mixture of rock and ice, with their density obtained from the $\rho - P$ relations presented in Hubbard & Marley (1989). We also included the effect of the stellar irradiation, assuming a zero albedo for the planet's radiative atmosphere, which is updated in steps of 500 Myr. Finally, we evolved different models, with different masses of the core, and we compared them with the position of TIC65910228b in the age–radius diagram. Figure 8 shows the position of TIC65910228b in the age–radius diagram, with different interior models. As can be seen, a model with solar composition for the envelope ($Z = 0.015$) and no core, is the one that better reproduces its position, suggesting a planet with very little heavy-elements content. We note, that the lightest possible model we could compute, that is, a pure H/He envelope with no core, does not match the 1- σ upper radius limit. On the other hand, a model with a massive core ($M_{\text{core}} = 160 M_{\oplus}$; $\rho_{\text{core}} = 16 [\text{g/cm}^3]$), matches the 1- σ lower limit. These results translate into a heavy-element enrichment with respect to the host star of $Z_p/Z_{\star} = 0.7^{+3.0}_{-0.7}$.

4.2. TIC65910228b in context

Physical parameters confirm a non-inflated radius, distinctive of a warm Jupiter. To provide context, we compare the obtained parameters with those of planets from the Exoplanet Archive¹ (Christiansen et al. 2025) with periods longer than $P = 10$ days and uncertainties lower than 20%.

In terms of mass and radius, TIC65910228b is similar to Kepler-432 b (Quinn et al. 2015), Kepler-1704 b (Dalba et al. 2021), TIC 241249530 b (Gupta et al. 2024), TIC 393818343 b (Sgro et al. 2024) and TOI-2497 b (Rodriguez et al. 2023), however, the first 4 planets orbit in very eccentric orbits ($e > 0.5$). TOI-2497 b has a similar mass, radius, and eccentricity, but has a period of $P = 10.65$ days, making TIC65910228b quite unique in this regime of mass. This comparison is illustrated in Figure 9, putting TIC65910228b close to the upper limit in mass of current discoveries.

In the period–eccentricity diagram (left panel Figure 10), we observe that TIC65910228b appears to be in an unpopulated region. If we add mass into the comparison, we identify TOI-4465 b (Essack et al. 2025) as a quite similar planet, but orbiting a G dwarf star. The color bar traces $\log g$ as a proxy with stellar evolution stage, showing that the current sample of planets around evolved stars has eccentric orbits (Grunblatt et al. 2023).

In the period–radius diagram (right panel Figure 10), we find that this planet is among the few warm Jupiters with an orbital period exceeding 100 days and a mild eccentricity, contrasting with some similar planets with much more eccentric orbits, as already stated in the previous paragraph.

Figure 11 shows the mass and eccentricity dependence on stellar metallicity. The left panel shows a well-known correlation where giant ($M > 0.1 M_J$) planets are observed around metal-rich stars (Gonzalez 1997; Fischer & Valenti 2005; Johnson et al. 2010). TIC65910228b is no exception to this

¹ Accessed on 2026-01-21 at 08:33 UT

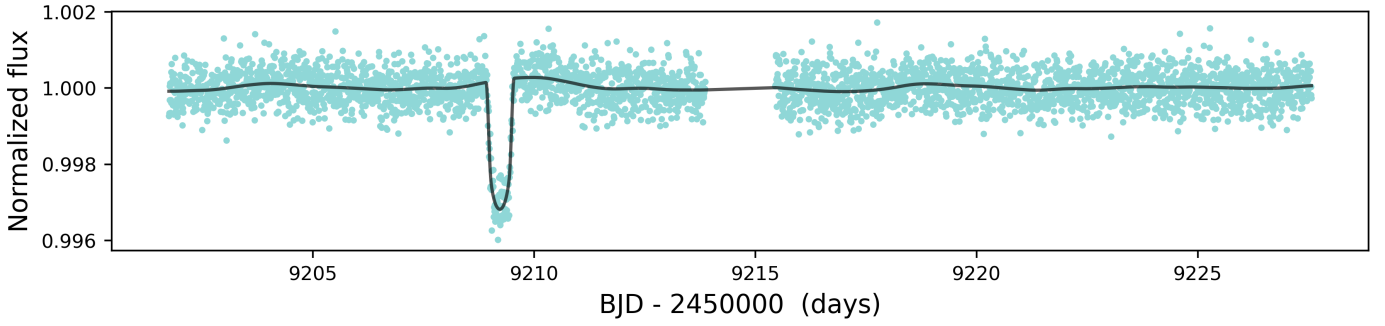


Fig. 4: Light curve of TESS Sector 33. The best-fit model is overplotted in black.

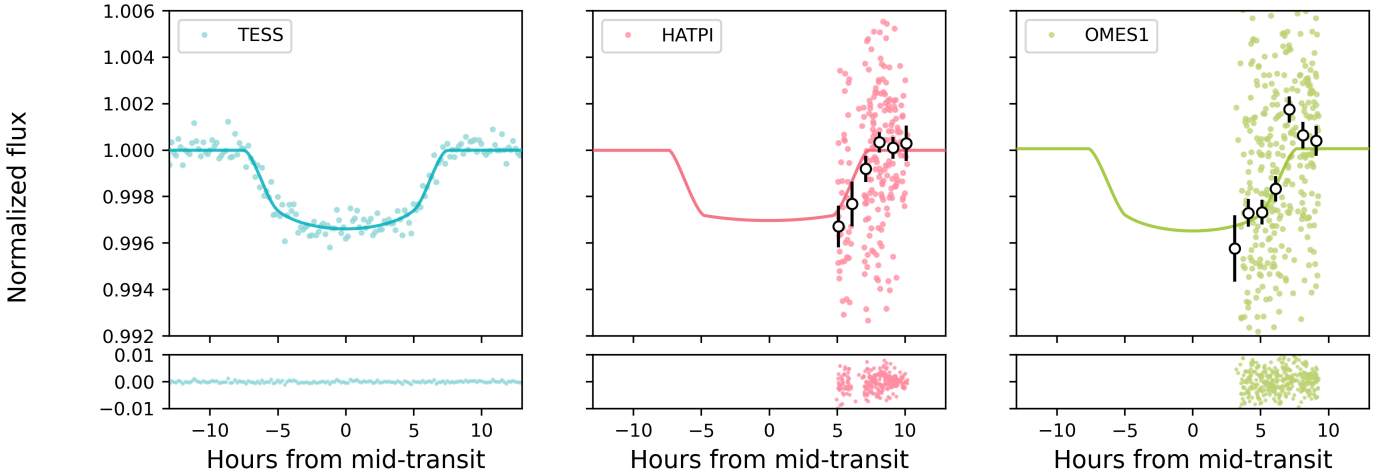


Fig. 5: Top panel: Observed transits with TESS, HATPI and OM-ES1, respectively. Model from joint-fit is overplotted. White circles correspond to 1-hour bins in HATPI and OMES1 light curves. Bottom panel: Residuals after removing the transit model.

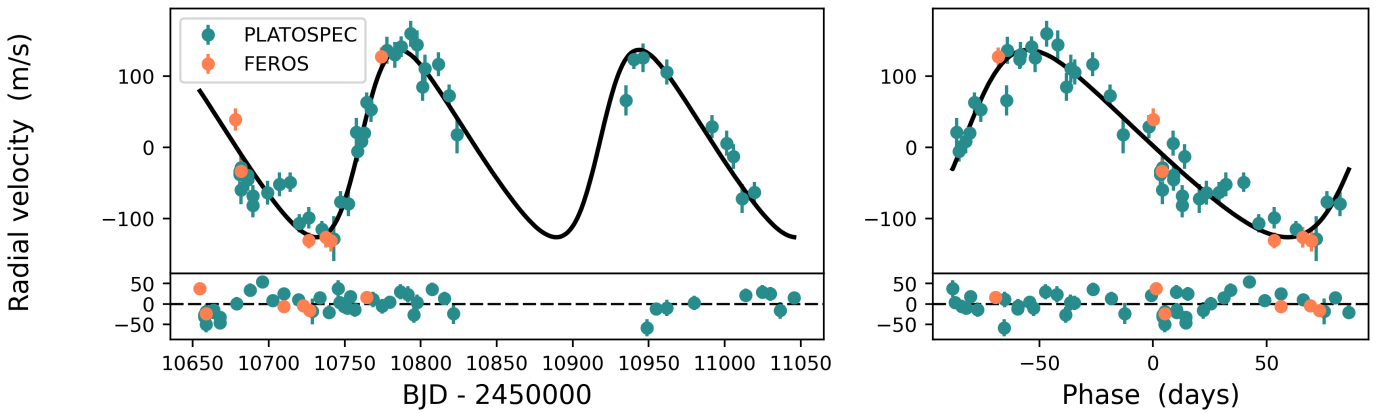


Fig. 6: Left panel: Radial velocities time series obtained with FEROS and PLATOSpec. Best model is plotted in black. Residuals after removing the Keplerian model are shown in bottom. Right panel: Same but phase folded radial velocities with the inferred period from the joint-fit.

trend, being in an interesting place, as its mass around $4.5 M_J$ is very close to a proposed break, where more massive planets tend to be hosted by lower metallicity stars (Schlaufman 2018; Goda & Matsuo 2019). This separation would be related to different formation channels: the core-accretion mechanism (Pollack et al. 1996) in the lower mass regime and disk instability (Boss 1997, 2024) for the most massive planets. The first mechanism is metallicity-dependent, and the second

one requires a massive disk (Matsuo et al. 2007). In contrast, Adibekyan (2019) doesn't find this separation in the giant planet population, but agrees on different formation mechanisms based on environmental conditions. The origin of giant planets with $M_P > 4 M_J$ remains a debated topic (Matsukoba et al. 2023; Nguyen & Adibekyan 2024).

The right panel of Figure 11 shows TIC65910228b in the metallicity-eccentricity space, where warm Jupiters

Parameter	Prior	Posterior	Units	Description
Star parameters				
ρ_\star	$\mathcal{N}(306, 8^2)$	$306.34^{+7.81}_{-7.87}$	kg m^{-3}	Stellar density
Planet parameters				
P_b	$\mathcal{N}(180.5, 0.5^2)$	$180.524140^{+0.000978}_{-0.001048}$	days	Orbital period
$t_{0,b}$	$\mathcal{N}(2459209.23, 0.5^2)$	$2459209.229716^{+0.002145}_{-0.002220}$	days	Time of transit center
$r_{1,b}$	$\mathcal{U}(0, 1)$	$0.8757^{+0.0133}_{-0.0173}$		Parametrization for p and b
$r_{2,b}$	$\mathcal{U}(0, 1)$	$0.0602^{+0.0019}_{-0.0022}$		Parametrization for p and b
K_b	$\mathcal{U}(0, 1000)$	$131.833^{+5.653}_{-5.866}$	m s^{-1}	Radial velocity semi-amplitude
e_b	$\mathcal{U}(0, 0.9)$	$0.25^{+0.03}_{-0.04}$		Orbital eccentricity
ω_b	$\mathcal{U}(0, 360)$	$279.13^{+3.31}_{-2.63}$	degrees	Argument of periapsis
Parameters for TESS				
D_{TESS}	1 (fixed)	1		Dilution factor for TESS
M_{TESS}	$\mathcal{N}(0, 0.001^2)$	$196^{+317}_{-327} \times 10^{-7}$		Relative flux offset for TESS
σ_{TESS}	$\mathcal{J}(10^{-1}, 10^4)$	2^{+13}_{-2}	ppm	Extra jitter term for TESS
$q_{1,\text{TESS}}$	$\mathcal{U}(0, 1)$	$0.519^{+0.248}_{-0.165}$		Quadratic limb-darkening parametrization
$q_{2,\text{TESS}}$	$\mathcal{U}(0, 1)$	$0.406^{+0.353}_{-0.274}$		Quadratic limb-darkening parametrization
$GP_{\sigma,\text{TESS}}$	$\mathcal{J}(10^{-6}, 10^6)$	$100^{+29}_{-19} \times 10^{-6}$		Amplitude of GP component
$GP_{\rho,\text{TESS}}$	$\mathcal{J}(10^{-6}, 10^6)$	$1.209^{+0.503}_{-0.335}$		ρ for GP component
Parameters for HATPI				
D_{HATPI}	$\mathcal{U}(0.8, 1)$	$0.904^{+0.062}_{-0.066}$		Dilution factor for HATPI
M_{HATPI}	$\mathcal{N}(0, 0.001^2)$	$46^{+233}_{-223} \times 10^{-7}$		Relative flux offset for HATPI
σ_{HATPI}	$\mathcal{J}(10^{-1}, 10^4)$	0^{+12}_{-0}	ppm	Extra jitter term for HATPI
$q_{1,\text{HATPI}}$	$\mathcal{U}(0, 1)$	$0.276^{+0.337}_{-0.200}$		Quadratic limb-darkening parametrization
$q_{2,\text{HATPI}}$	$\mathcal{U}(0, 1)$	$0.431^{+0.352}_{-0.308}$		Quadratic limb-darkening parametrization
Parameters for OM-ES1				
D_{OMES1}	1 (fixed)	1		Dilution factor for OM-ES1
M_{OMES1}	$\mathcal{N}(0, 0.001^2)$	$2327^{+1671}_{-1663} \times 10^{-7}$		Relative flux offset for OM-ES1
σ_{OMES1}	$\mathcal{J}(10^{-1}, 10^4)$	1^{+180}_{-1}	ppm	Extra jitter term for OM-ES1
$q_{1,\text{OMES1}}$	$\mathcal{U}(0, 1)$	$0.574^{+0.265}_{-0.279}$		Quadratic limb-darkening parametrization
$q_{2,\text{OMES1}}$	$\mathcal{U}(0, 1)$	$0.406^{+0.315}_{-0.291}$		Quadratic limb-darkening parametrization
RV parameters				
μ_{FEROS}	$\mathcal{U}(20000, 20100)$	20027^{+7}_{-8}	m s^{-1}	Systemic velocity for FEROS
σ_{FEROS}	$\mathcal{J}(10^{-1}, 10^2)$	7^{+17}_{-6}	m s^{-1}	Extra jitter term for FEROS
$\mu_{\text{PLATOSPEC}}$	$\mathcal{U}(20000, 20100)$	20063^{+4}_{-4}	m s^{-1}	Systemic velocity for PLATOSpec
$\sigma_{\text{PLATOSPEC}}$	$\mathcal{J}(10^{-1}, 10^2)$	19^{+4}_{-4}	m s^{-1}	Extra jitter term for PLATOSpec

Table 3: Priors used for the joint analysis of TIC65910228b. \mathcal{U} , \mathcal{J} and \mathcal{N} represent uniform, log-uniform and normal distributions, respectively. Posterior values obtained are listed in the adjacent column.

exhibit a wider range of eccentricities at high metallicities (Dawson & Murray-Clay 2013; Alqasim et al. 2025; Morgan et al. 2026). TIC65910228b occupies a mid value in this range, and confirming the presence of unseen companions and/or a study of the obliquity would provide a better constraint on the migration scenario of this planet.

The interior modeling indicates a low level of heavy-element enrichment on this planet, similar to other massive giant planets, such as TIC4672985 b (Jones et al. 2024). Additionally, the coreless model suggests that this planet may have formed through gravitational instability.

4.3. Future observations

The orbital obliquity can be measured through the Rossiter-McLaughlin (RM) effect (Rossiter 1924; McLaughlin 1924; Triaud 2018), which provides insight into the planet's migration scenarios (Petrovich & Tremaine 2016). In principle, an aligned orbit points to a disk migration scenario; meanwhile, a misaligned orbit hints at a previous interaction with a companion (Winn 2010). We estimate the amplitude of the RM effect to be 12.3 ± 1 m/s, which should be attainable with current state-of-the-art instruments from the southern hemisphere. Nevertheless, the 11.6-hour transit duration makes this study quite expensive and difficult to observe.

We also calculated the transmission spectroscopy metric (TSM Kempton et al. 2018), which quantifies a planet's poten-

Parameter name	Posterior estimate	Description
Transit parameter		
R_p/R_\star	$0.0602^{+0.0022}_{-0.0019}$	Planetary radius to star radius
b	$0.8135^{+0.0200}_{-0.0260}$	Transit impact parameter
a/R_\star	$80.812^{+0.680}_{-0.698}$	Normalized semi-major axis
i (deg)	$89.53^{+0.01}_{-0.01}$	Orbital inclination
t_T (hour)	$11.61^{+0.47}_{-0.41}$	Transit duration
Planet parameter		
M_p (M_J)	$4.554^{+0.255}_{-0.247}$	Mass
R_p (R_J)	$1.088^{+0.061}_{-0.057}$	Radius
ρ_p (g cm^{-3})	$4.374^{+0.800}_{-0.674}$	Bulk density
g_p (m s^{-2})	$95.1^{+11.8}_{-10.4}$	Surface gravity
a (AU)	$0.697^{+0.011}_{-0.012}$	Semi-major axis
T_{eq} (K)	582^{+8}_{-8}	Equilibrium temperature

Table 4: Transit and planetary parameters derived from the joint-fit. Median and 68% confidence intervals from the posteriors are reported.

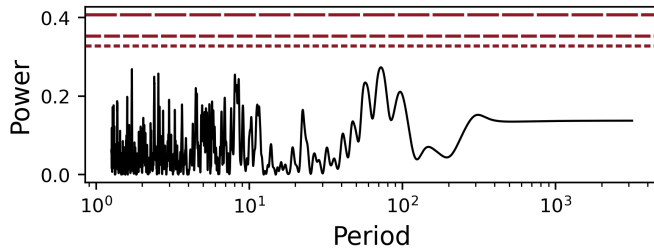


Fig. 7: GLS periodogram of radial velocity residuals after removing the best fit model. Given the current data and time baseline, no significant peaks are found.

tial for atmospheric studies. It's important to note that this metric is defined with a scale factor that accommodates planets up to 10 Earth masses. Therefore, we compute it using the scale factor from the last bin. The resulting TSM is 3.44, which falls in the lower range, making TIC65910228b not a good candidate for atmospheric studies, despite its relevance due to its cooler equilibrium temperature (Fortney et al. 2021). This outcome can be attributed to the planet's low equilibrium temperature T_{eq} along with its higher mass M_p and star radius R_\star .

Finally, we calculated the emission spectroscopy metric (ESM Kempton et al. 2018), which is similar to TSM but focused on the expected signal-to-noise (SNR) ratio for thermal emission characterization using the James Webb Space Telescope (JWST). For TIC65910228b, we obtain an ESM value of 4.8, which is below the recommended SNR of 7.5 for this kind of study.

5. Conclusions

Starting from a single transit event and following up with ground-based photometric and spectroscopic observations, we report the discovery and characterization of TIC65910228b, a long-period warm Jupiter orbiting an evolved F-type star. With a period of $180.524140^{+0.000978}_{-0.001048}$ days, mass of $4.554^{+0.255}_{-0.247} M_J$, radius of $1.088^{+0.061}_{-0.057} R_J$, eccentricity of $0.25^{+0.03}_{-0.04}$, and equilibrium

temperature of 582^{+8}_{-8} K, TIC65910228b joins the scarce population of warm Jupiters with periods longer than 100 days.

The Rossiter-McLaughlin amplitude of 12 m/s for this planet is suitable for observations with current facilities in terms of precision; however, the 11.6-hour transit duration makes it very challenging to observe in a single night. A low obliquity, pointing to an aligned orbit, would be quite significant, as it would support a disk-migration origin; meanwhile, most long-period warm Jupiters have extreme eccentricities, which are more related to a planet-planet scattering scenario.

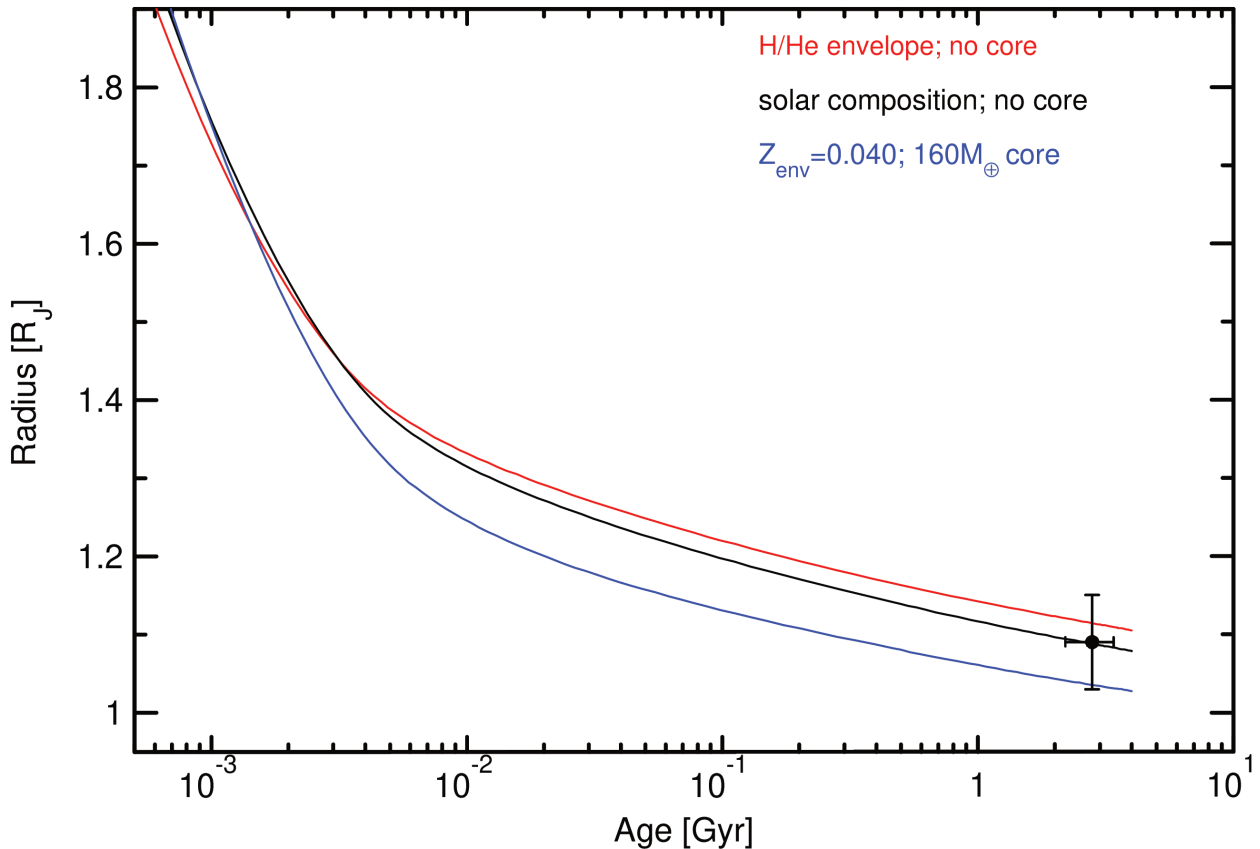


Fig. 8: Position of TIC65910228 *b* in the age-radius diagram (black dot). Different interior models with different envelope composition and core masses over-plotted.

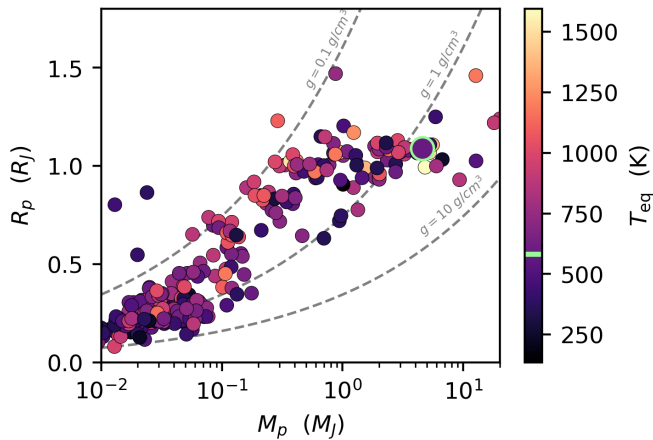


Fig. 9: Mass vs radius diagram for confirmed planets with $P > 10$ days. Circles are colored according to each planet's equilibrium temperature reported in the catalog.

Acknowledgements. An independent study to confirm and characterize TIC65910228b was carried out and submitted simultaneously by Rodel et al. 2026, in prep. This work has made use of data from the European Space Agency (ESA) mission *Gaia* (<https://www.cosmos.esa.int/gaia>), processed by the *Gaia* Data Processing and Analysis Consortium (DPAC, <https://www.cosmos.esa.int/web/gaia/dpac/consortium>). Funding for the DPAC has been provided by national institutions, in particular the institutions participating in the *Gaia* Multilateral Agreement. This paper makes use of data produced

by the HATPI project (<https://hatpi.org>), located in Chile at Las Campanas Observatory of the Carnegie Institution for Science and operated by the Department of Astrophysical Sciences at Princeton University. External funding for HATPI has been provided by the Gordon and Betty Moore Foundation, the David and Lucile Packard Foundation, the Mount Cuba Astronomical Foundation, and the Agencia Nacional de Investigación y Desarrollo (ANID) of Chile through QUIMAL, Millennium and Fondecyt grants. FR acknowledges the support from the Vicerrectoría de Investigación (VRI) at the Pontificia Universidad Católica de Chile. RB acknowledges support from FONDECYT Project 1241963 and from ANID – Millennium Science Initiative – ICN12_009. JJ is grateful that the publication could be produced within the framework of institutional support for the development of the research organization of Masaryk University. LV acknowledges the support from ANID Fondecyt no. 1211162, Fondecyt no. 1251299, and BASAL FB210003.

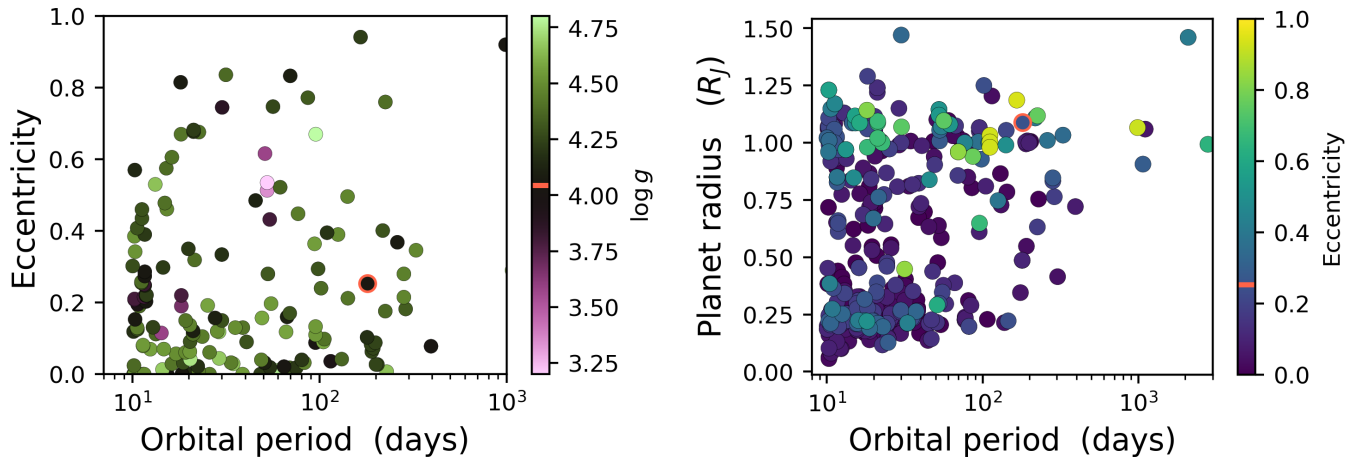


Fig. 10: Planets with $P > 10$ days and their orbital period vs eccentricity and planetary radii. The left panel shows the dependency of orbital period on eccentricity. $\log g$ is plotted in color scale. The right panel shows the period-radius diagram with TIC65910228b being one of the longer period giant planets discovered.

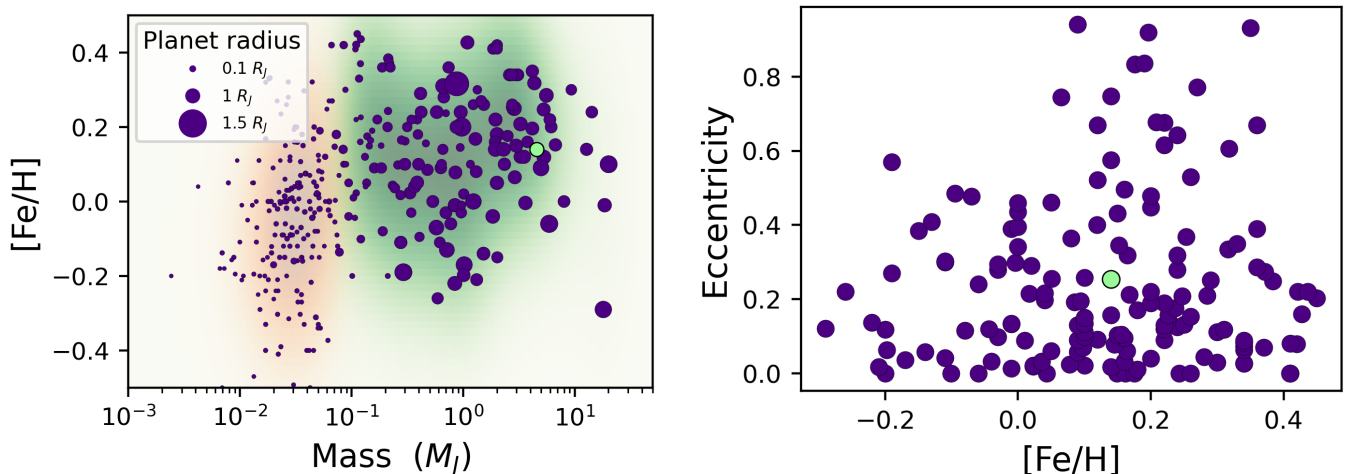


Fig. 11: Left: Mass vs stellar metallicity diagram for planets with $P > 10$ d. Kernel density estimation for planets with mass lower and higher than $0.1 M_J$ are plotted for reference. Right: Metallicity vs eccentricity diagram for planets with $P > 10$ d and $M > 0.1 M_J$. TIC65910228b is shown in green in both panels.

References

Acuña, L., Kreidberg, L., Zhai, M., & Mollière, P. 2024, A&A, 688, A60
 Adibekyan, V. 2019, Geosciences, 9, 105
 Albrecht, S. H., Dawson, R. I., & Winn, J. N. 2022, PASP, 134, 082001
 Alqasim, A., Hirano, T., Hori, Y., et al. 2025, MNRAS, 539, 307
 Ambikasaran, S., Foreman-Mackey, D., Greengard, L., Hogg, D. W., & O’Neil, M. 2015, IEEE Transactions on Pattern Analysis and Machine Intelligence, 38, 252
 Boley, A. C., Granados Contreras, A. P., & Gladman, B. 2016, ApJ, 817, L17
 Boss, A. P. 1997, Science, 276, 1836
 Boss, A. P. 2024, ApJ, 969, 157
 Brahm, R., Espinoza, N., Jordán, A., et al. 2019, AJ, 158, 45
 Brahm, R., Jordán, A., & Espinoza, N. 2017a, PASP, 129, 034002
 Brahm, R., Jordán, A., Hartman, J., & Bakos, G. 2017b, MNRAS, 467, 971
 Brahm, R., Ulmer-Moll, S., Hobson, M. J., et al. 2023, AJ, 165, 227
 Bressan, A., Marigo, P., Girardi, L., et al. 2012, MNRAS, 427, 127
 Caldwell, D. A., Tenenbaum, P., Twicken, J. D., et al. 2020, Research Notes of the American Astronomical Society, 4, 201
 Christiansen, J. L., McElroy, D. L., Harbut, M., et al. 2025, PSJ, 6, 186
 Cooke, B. F., Pollacco, D., West, R., McCormac, J., & Wheatley, P. J. 2018, A&A, 619, A175
 Dalba, P. A., Kane, S. R., Li, Z., et al. 2021, AJ, 162, 154
 Dawson, R. I. & Murray-Clay, R. A. 2013, ApJ, 767, L24
 Eberhardt, J., Trifonov, T., Henning, T., et al. 2025, AJ, 169, 298
 Espinoza, N. 2018, Research Notes of the American Astronomical Society, 2, 209
 Espinoza, N. & Jordán, A. 2016, MNRAS, 457, 3573
 Essack, Z., Dragomir, D., Dalba, P. A., et al. 2025, AJ, 170, 41
 Fischer, D. A. & Valenti, J. 2005, ApJ, 622, 1102
 Foreman-Mackey, D., Agol, E., Angus, R., & Ambikasaran, S. 2017, ArXiv
 Fortney, J., Visscher, C., Marley, M., et al. 2021, in American Astronomical Society Meeting Abstracts #237, 111.04
 Fulton, B. J., Petigura, E. A., Blunt, S., & Sinukoff, E. 2018, PASP, 130, 044504
 Gaia Collaboration, Brown, A. G. A., Vallenari, A., et al. 2021, A&A, 649, A1
 Gaia Collaboration, Vallenari, A., Brown, A. G. A., et al. 2023, A&A, 674, A1
 Goda, S. & Matsuo, T. 2019, ApJ, 876, 23
 Goldreich, P. & Tremaine, S. 1980, ApJ, 241, 425
 Gonzalez, G. 1997, MNRAS, 285, 403
 Grunblatt, S. K., Saunders, N., Chontos, A., et al. 2023, AJ, 165, 44
 Gupta, A. F., Millholland, S. C., Im, H., et al. 2024, Nature, 632, 50
 Høg, E., Fabricius, C., Makarov, V. V., et al. 2000, A&A, 355, L27
 Hubbard, W. & Marley, M. S. 1989, Icarus, 78, 102
 Johnson, J. A., Aller, K. M., Howard, A. W., & Crepp, J. R. 2010, PASP, 122, 905
 Jones, M. I., Reinarz, Y., Brahm, R., et al. 2024, A&A, 683, A192
 Kabáth, P., Skarka, M., Hatzes, A., et al. 2025, arXiv e-prints, arXiv:2510.11961

Kaufer, A., Stahl, O., Tubbesing, S., et al. 1999, *The Messenger*, 95, 8

Kempton, E. M.-R., Bean, J. L., Louie, D. R., et al. 2018, *PASP*, 130, 114401

Kipping, D. M. 2010, *MNRAS*, 408, 1758

Kipping, D. M. 2013, *MNRAS*, 435, 2152

Kovács, G., Bakos, G., & Noyes, R. W. 2005, *MNRAS*, 356, 557

Kozai, Y. 1962, *AJ*, 67, 591

Kreidberg, L. 2015, batman: BAsic Transit Model cAlculatioN in Python, *Astrophysics Source Code Library*, record ascl:1510.002

Lidov, M. L. 1962, *Planet. Space Sci.*, 9, 719

Lithwick, Y. & Wu, Y. 2011, *ApJ*, 739, 31

Matsukoba, R., Vorobyov, E. I., Hosokawa, T., & Guedel, M. 2023, *MNRAS*, 526, 3933

Matsuo, T., Shibai, H., Ootsubo, T., & Tamura, M. 2007, *ApJ*, 662, 1282

Mayor, M. & Queloz, D. 1995, *Nature*, 378, 355

McLaughlin, D. B. 1924, *ApJ*, 60, 22

Morgan, M., Bowler, B. P., & Tran, Q. H. 2026, *AJ*, 171, 19

Nguyen, M. & Alibekyan, V. 2024, *Ap&SS*, 369, 122

Paxton, B., Bildsten, L., Dotter, A., et al. 2011, *ApJS*, 192, 3

Paxton, B., Cantiello, M., Arras, P., et al. 2013, *ApJS*, 208, 4

Petrovich, C. & Tremaine, S. 2016, *ApJ*, 829, 132

Pollack, J. B., Hubickyj, O., Bodenheimer, P., et al. 1996, *Icarus*, 124, 62

Quinn, S. N., White, T. R., Latham, D. W., et al. 2015, *ApJ*, 803, 49

Rasio, F. A. & Ford, E. B. 1996, *Science*, 274, 954

Ricker, G. R., Winn, J. N., Vanderspek, R., et al. 2014, in *Society of Photo-Optical Instrumentation Engineers (SPIE) Conference Series*, Vol. 9143, *Space Telescopes and Instrumentation 2014: Optical, Infrared, and Millimeter Wave*, ed. J. M. Oschmann, Jr., M. Clampin, G. G. Fazio, & H. A. MacEwen, 914320

Rodel, T., Bayliss, D., Gill, S., & Hawthorn, F. 2024, *MNRAS*, 529, 715

Rodríguez, J. E., Quinn, S. N., Vanderburg, A., et al. 2023, *MNRAS*, 521, 2765

Rossiter, R. A. 1924, *ApJ*, 60, 15

Sarkis, P., Mordasini, C., Henning, T., Marleau, G. D., & Mollière, P. 2021, *A&A*, 645, A79

Schlaufman, K. C. 2018, *ApJ*, 853, 37

Sgro, L. A., Dalba, P. A., Esposito, T. M., et al. 2024, *AJ*, 168, 26

Skilling, J. 2004, in *American Institute of Physics Conference Series*, Vol. 735, *Bayesian Inference and Maximum Entropy Methods in Science and Engineering: 24th International Workshop on Bayesian Inference and Maximum Entropy Methods in Science and Engineering*, ed. R. Fischer, R. Preuss, & U. V. Toussaint (AIP), 395–405

Skrutskie, M. F., Cutri, R. M., Stiening, R., et al. 2006, *AJ*, 131, 1163

Speagle, J. S. 2020, *MNRAS*, 493, 3132

Stassun, K. G., Oelkers, R. J., Pepper, J., et al. 2018, *AJ*, 156, 102

Tala Pinto, M., Jordán, A., Acuña, L., et al. 2025, *A&A*, 694, A268

Tayar, J., Clayton, Z. R., Huber, D., & van Saders, J. 2022, *ApJ*, 927, 31

Thorngren, D. P., Fortney, J. J., Murray-Clay, R. A., & Lopez, E. D. 2016, *ApJ*, 831, 64

Triaud, A. H. M. J. 2018, in *Handbook of Exoplanets*, ed. H. J. Deeg & J. A. Belmonte, 2

Villanueva, Jr., S., Dragomir, D., & Gaudi, B. S. 2019, *AJ*, 157, 84

Winn, J. N. 2010, in *Exoplanets*, ed. S. Seager, 55–77

Zechmeister, M. & Kürster, M. 2009, *A&A*, 496, 577

¹ Instituto de Astrofísica, Pontificia Universidad Católica de Chile, Av. Vicuña Mackenna 4860, 7820436 Macul, Santiago, Chile
e-mail: firojas@uc.cl

² Facultad de Ingeniería y Ciencias, Universidad Adolfo Ibáñez, Av. Diagonal las Torres 2640, Peñalolén, Santiago, Chile

³ Millennium Institute for Astrophysics, Nuncio Monseñor Sotero Sanz 100, Of. 104, Providencia, Santiago, Chile

⁴ European Southern Observatory (ESO), Alonso de Córdova 3107, Vitacura, Casilla 19001, Santiago, Chile

⁵ Max-Planck-Institut für Astronomie, Königstuhl 17, D-69117 Heidelberg, Germany

⁶ Space Telescope Science Institute, 3700 San Martin Drive, Baltimore, MD 21218, USA

⁷ Astronomical Institute of the Czech Academy of Sciences, Fričova 298, CZ-25165 Ondřejov, Czech Republic

⁸ Astronomical Institute of Charles University, V Holešovičkách 2, CZ-180 00 Prague, Czech Republic

⁹ Department of Astronomy, McPherson Laboratory, The Ohio State University, 140 W 18th Ave, Columbus, Ohio 43210, USA

¹⁰ Department of Astronomy, Sofia University “St Kliment Ohridski”, 5 James Bourchier Blvd, BG-1164 Sofia, Bulgaria

¹¹ Landessternwarte, Zentrum für Astronomie der Universität Heidelberg, Königstuhl 12, D-69117 Heidelberg, Germany

¹² Department of Theoretical Physics and Astrophysics, Faculty of Science, Masaryk University, Kotlářská 2, CZ-61137 Brno, Czech Republic

¹³ Center of Astro Engineering, Pontificia Universidad Católica de Chile, Av. Vicuña Mackenna 4860, 782-043 Santiago, Chile

¹⁴ Department of Electrical Engineering, Pontificia Universidad Católica de Chile, Av. Vicuña Mackenna 4860, 782-043 Santiago, Chile

¹⁵ Department of Astrophysical Sciences, Princeton University, 4 Ivy Lane, Princeton, NJ 08544, USA

¹⁶ El Sauce Observatory — Obstech, Coquimbo, Chile

¹⁷ Cavendish Laboratory, J. J. Thomson Avenue, Cambridge, CB3 0HE, UK

¹⁸ Thüringer Landessternwarte, D-07778 Tautenburg, Germany

¹⁹ Western Connecticut State University, Danbury, CT 06810, USA

²⁰ Denys Wilkinson Building, Department of Physics, University of Oxford, OX1 3RH, UK

²¹ Institute of Plasma Physics of the CAS, TOPTEC department, U Slovany 2525/1a 182 00 Prague 8, Libeň, Czech Republic